Journal of Marine Science and Engineering

MDPI

Article

Effect of Starting Conditions on the Internal Flow Field and Interior Ballistic Performance of an Underwater Ventilated Launch

Xinwei Zhang [1], Yubo Hu [2] and Yonggang Yu [1,*]

[1] School of Energy and Power Engineering, Nanjing University of Science and Technology, Nanjing 210094, China; zxwnjust@163.com
[2] The Third Research Department, Xi'an Modern Chemistry Research Institute, Xi'an 710065, China; 15251820423@163.com
* Correspondence: yygnjust801@163.com

Abstract: As one of the future main directions for underwater artillery, a ventilated launch can significantly reduce the huge water resistance during the underwater launching process. This paper aims to clarify the effect of starting conditions on the internal flow field and interior ballistic performance of an underwater ventilated launcher. Firstly, a three-dimensional unsteady model of gas–liquid two-phase flow is established. Following, an interior ballistic program of the underwater ventilated launch is developed. A coupling model between interior ballistic and gas–liquid interaction is then established, accounting for the projectile's dynamic boundary effect and gas–liquid interaction. Subsequently, the simulation accuracy of the model is confirmed. Finally, the effect of parameter adjustments on the internal flow field and interior ballistic properties are contrasted and examined by altering the starting conditions. The results indicate that adjusting the gas injection pressure and projectile starting pressure can effectively regulate the drainage and resistance reduction effect, thereby obtaining the desired interior ballistic performance of the underwater ventilated launch. The findings offer recommendations for future underwater launchers.

Keywords: underwater launch; gas–liquid interaction; flow field; interior ballistic; drag reduction

check for updates

Citation: Zhang, X.; Hu, Y.; Yu, Y. Effect of Starting Conditions on the Internal Flow Field and Interior Ballistic Performance of an Underwater Ventilated Launch. *J. Mar. Sci. Eng.* **2023**, *11*, 1525. https://doi.org/10.3390/jmse11081525

Academic Editor: Alon Gany

Received: 28 June 2023
Revised: 22 July 2023
Accepted: 25 July 2023
Published: 31 July 2023

Copyright: © 2023 by the authors. Licensee MDPI, Basel, Switzerland. This article is an open access article distributed under the terms and conditions of the Creative Commons Attribution (CC BY) license (https://creativecommons.org/licenses/by/4.0/).

1. Introduction

Developing highly effective low-resistance underwater artillery is one of the crucial objectives for researchers, which is also an urgent need for the Navy. It is well known that water has an approximate 800-fold higher density than air, making vehicles submerged in water far more difficult to navigate than that in air. Thus, reducing the drag of vehicles has long been one of the issues of greatest concern in underwater launch. Supercavitation technology [1–3] is a ground-breaking method of reducing drag in the water that has much of attention. It encases the underwater vehicle in a gas cavity via artificial ventilation or natural cavitation, preventing contact between the vehicle's side and the water. This can considerably lower the viscous resistance of the vehicle during underwater navigation, allowing for optimal speed and range. However, the only vehicles that can use it are those that have already moved in water and are incapable of being propelled by a launch tube. For vehicles that need to be launched underwater, supercavitation technology will not be effective when moving inside the launch tube. Ventilation can still be used to reduce drag, such as submarine launched missiles. For underwater missiles, ventilation can also be used to reduce resistance and improve underwater launch performance during their launching and navigation processes [4–6].

However, the only way for underwater artillery to achieve a high muzzle velocity is precisely to reduce the resistance during the launch process, as the initial velocity of the projectile often reaches 800–1000 m/s. For submerged underwater guns, the water inside the barrel has a significant negative impact on the firing performance and safety. In order to improve muzzle velocity and ensure shooting safety, Wang's team [7] adopt a shortened barrel to reduce added mass for better interior ballistic performance. Of course, a sealing structure [8] can also be adopted to make sure that no water can enter the barrel, thereby achieving low-resistance launch of underwater guns. Each of these approaches, nevertheless, have substantial drawbacks. First, shortening the barrel only accomplishes low-resistance launch by reducing the added mass, which also shortens the projectile's acceleration distance, lowering its muzzle velocity. This is due to the fact that it does not significantly alter the launch environment. Secondly, the sealing device increases the complexity of the mechanical structure, making it difficult to adapt to the harsh underwater high-frequency launch combat environment [9]. In recent years, we have proposed the underwater ventilated launch to address the drawbacks of sealed launch and submerged launch based on the structure design of projectile and barrel. Through reasonable charge design, it is possible to achieve low-resistance and high-velocity launch of underwater guns [10,11]. Hu [12] built a simulated projectile with circumferential grooves attached to the wall in order to explore the joint draining capabilities of numerous wall gas jets. Zhao [13] created a simulated projectile with one vertical central nozzle and four to eight slant lateral nozzles, and then used experiment and numerical simulation to determine the main factors influencing gas–liquid turbulent mixing downstream. To clarify the effect of side and center nozzle sizes on the evolution characteristics and drag-reduction effect of the gas-curtain, an underwater simulated-launch experimental device was constructed and experimental study under multiple operating conditions were conducted by Zhou [14]. Our team [15,16] has also designed a ventilated launch mechanism with grooves in the inner wall of the barrel to avoid lowering the structural strength of the projectile. The effect of the groove structure on the independent expansion and interference properties of multiple jets is thus numerically investigated.

The schematic diagram of the ventilated launcher with grooves in the inner wall of the barrel is shown in Figure 1. Firstly, the coated propellant inside the chamber is ignited. The projectile belt is squeezed into the barrel for a short distance to connect the chamber and the barrel with grooves once the gas pressure inside the chamber reaches a specific value. However, due to the poor burning rate of the propellant coating layer, the volume of gas generated is relatively tiny, and a portion cannot engage in the work on the projectile, causing the projectile to stagnate for a short period of time. As the gas in the chamber blasts from the slit between the projectile and the barrel towards the projectile's front, several gas jets form a gas-curtain to force away the water in the barrel. While the propellant coating layer is totally burned off, the propellant matrix rapidly burns to produce a large amount of high-temperature and high-pressure gas, which drives the projectile to move at high speed in a low-resistance environment.

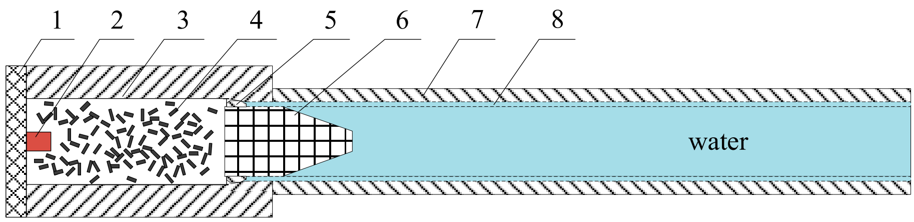

Figure 1. Schematic diagram of underwater ventilated launch. 1—breech, 2—igniter, 3—chamber, 4—propellant, 5—belt, 6—projectile, 7—barrel, 8—groove.

It is clear that altering factors such as the belt parameters, the gas-curtain drainage efficiency, and interior ballistic performance can be controlled. To further master the interior ballistic control technology of ventilated launch, the drainage effectiveness and interior ballistic performance under diverse starting conditions are the main topics of this paper. In order to achieve the expected goals, a matching design was carried out between the charge and the projectile-gun structure, using coated propellants to meet the needs of gas-curtain drainage and high-speed propulsion, and a jet structure was designed to achieve real-time drainage and drag reduction. This study is of great significance for achieving efficient and controllable launch of underwater guns.

2. Theoretical Model

A range of sophisticated physical and chemical processes, such as propellant combustion and gas flow in narrow grooves, gas–liquid interaction, projectile motion, turbulence, and so on, are involved in the underwater ventilated launch process. The theoretical model for the ventilated launch including the above process is established as follows.

2.1. Physical Assumptions

(1) The propellant obeys the parallel layer combustion rule. The propellant surface catches fire at the same time. All of the surfaces burn at the same speed, and the burning surface recedes at the same speed.
(2) The gas is compressible and conforms to the Nobel–Abel equation.
(3) Without taking into account the process of the projectile belt compression, the projectile starts to move once the combustion chamber pressure reaches the projectile's starting pressure.
(4) The RNG k-ε model is employed to describe the turbulent mixing of gas and liquid while the endothermic evaporation of liquid is disregarded.
(5) The volume of fluid (VOF) method is applied to capture the boundary of the gas-curtain.

2.2. Governing Equations

In general, the model of ventilated launch mainly includes an interior ballistic model, a turbulence model [17,18], and governing equations for gas–liquid flow [19,20].

The thorough introduction of the interior ballistic equations is given below.

(1) Expression for the proportion of propellant combustion:

$$\psi = \begin{cases} B\left(1 + \frac{e_1}{\Delta e_\mathrm{b}} Z\right),\ -\frac{\Delta e_\mathrm{b}}{e_1} \leqslant Z < 0 \\ B + \chi_\mathrm{p} Z\left(1 + \lambda_\mathrm{p} Z + \mu_\mathrm{p} Z^2\right)(1 - B),\ 0 \leqslant Z < 1 \\ B + \chi_\mathrm{s} Z(1 + \lambda_\mathrm{s} Z)(1 - B),\ 1 \leqslant Z < Z_\mathrm{k} \\ 1,\ Z = Z_\mathrm{k} \end{cases} \tag{1}$$

ψ is the proportion of burned propellant; B is the proportion of coating layer mass; e_1 is half the thickness of the propellant arc; Δe_b is the thickness of the coating layer; Z represents the relative thickness burned according to the parallel layer theory; χ_p, λ_p, μ_p, χ_s, and λ_s are the feature parameters related to propellant shape; and Z_k is the relative thickness after the propellant has split and all of its pieces have been burned.

Here, $Z < 0$ represents the combustion of the propellant coating layer, and $Z \geq 0$ represents the combustion of the propellant matrix.

(2) Exponential burning rate equation:

$$\frac{\mathrm{d}Z}{\mathrm{d}t} = \begin{cases} \frac{u_\mathrm{b}}{e_1} {p_\mathrm{c}}^{n_\mathrm{p}},\ Z < 0 \\ \frac{u_\mathrm{p}}{e_1} {p_\mathrm{c}}^{n_\mathrm{p}},\ 0 \leqslant Z < Z_\mathrm{k} \\ 0,\ Z = Z_\mathrm{k} \end{cases} \tag{2}$$

In the exponential combustion law, n and u represent the burning rate index and coefficient, respectively. The propellant coating layer and matrix, respectively, are denoted by the subscripts "b" and "p", and p_c is the chamber pressure.

(3) Equation of gas state:

$$p_\mathrm{c}\left(\frac{1}{\rho_\mathrm{g}} - \alpha_\mathrm{p}\right) = R_\mathrm{g} T_\mathrm{c} \tag{3}$$

R_g stands for the constant of the combustion gas and T_c for the temperature of the gas; α_p is the gas covolume, which is a correction to the state equation of high-pressure combustion gas.

(4) Momentum equation:

$$\varphi m \frac{dv_p}{dt} = S_0 p_c - F_w \tag{4}$$

S_0 is the cross-sectional area of the projectile; φ represents the proportional coefficient between secondary work and kinetic energy of the projectile; m and v_p are the mass and velocity of the projectile; and F_w is the motion resistance of the projectile.

(5) Motion equation of the projectile:

$$\frac{dl}{dt} = v_p \tag{5}$$

l is the displacement of the projectile.

(6) Energy equation:

$$S_0 p_c (l_\psi + l) = \begin{cases} \frac{f_b \omega_b \psi}{B} - \theta_p \left(\frac{1}{2} m \varphi v_p{}^2 + \int_0^t q_m u_g dt + \int_0^l F_w dl \right), \; Z < 0 \\ \omega_b \left[f_p \left(\frac{\psi}{B} - 1 \right) + f_b \right] - \theta_p \left(\frac{1}{2} m \varphi v_p{}^2 + \int_0^t q_m u_g dt + \int_0^l F_w dl \right), \; Z \geqslant 0 \end{cases} \tag{6}$$

f is the propellant impetus; ω is the propellant mass; k_p is the specific heat ratio of gas; q_m and u_g are the mass of gas flowing out of the chamber and the internal energy carried by it per unit time, respectively; l_0 is the initial chamber length; Δ is the charge density of the propellant; and V_0 is the initial volume of the chamber.

(7) Gas flow equation:

$$q_m = \begin{cases} \varphi_1 \frac{p_c S}{\sqrt{f \tau_1}} \left(\frac{2}{k+1} \right)^{\frac{k+1}{2(k-1)}} \sqrt{k}, & \frac{p}{p_c} \leq \left(\frac{2}{k+1} \right)^{\frac{k}{k-1}} \\ \varphi_t \frac{p_c S}{\sqrt{f \tau_1}} \sqrt{ \frac{2k}{k-1} \left[\left(\frac{p}{p_c} \right)^{\frac{2}{k}} - \left(\frac{p}{p_c} \right)^{\frac{k+1}{k}} \right] }, & \frac{p}{p_c} > \left(\frac{2}{k+1} \right)^{\frac{k}{k-1}} \end{cases} \tag{7}$$

φ_1 is the correction coefficient of the gas flow; S is the grooves' cross-sectional area; and τ_1 is the gas temperature in the chamber.

3. Numerical Methods and Initial Boundary Conditions

A fourth-order Runge–Kutta method is used to solve the interior ballistic model of the ventilated launch [21,22]. The gas–liquid flow field solution is based on the CFD software FLUENT. A user-defined function (UDF) is used to compile the interior ballistic program into FLUENT software. Figure 2 depicts the FLUENT and UDF coupling solution procedure.

Before starting the numerical simulation, the boundary conditions are set and the flow field initialized based on the actual situation. Then, FLUENT calculates the pressures at various locations in the flow field and transmits the pressure at projectile head and base to the user-defined function. Next, the interior ballistic program obtains the projectile velocity and the chamber pressure. At this point, the interior ballistic program determines whether the projectile has exited the barrel. If the projectile has exited the barrel, the calculation stops. Otherwise, the user-defined function feeds back the projectile velocity to the dynamic grid and applies the chamber pressure to the pressure inlet. Subsequently, FLUENT begins the next iteration calculation.

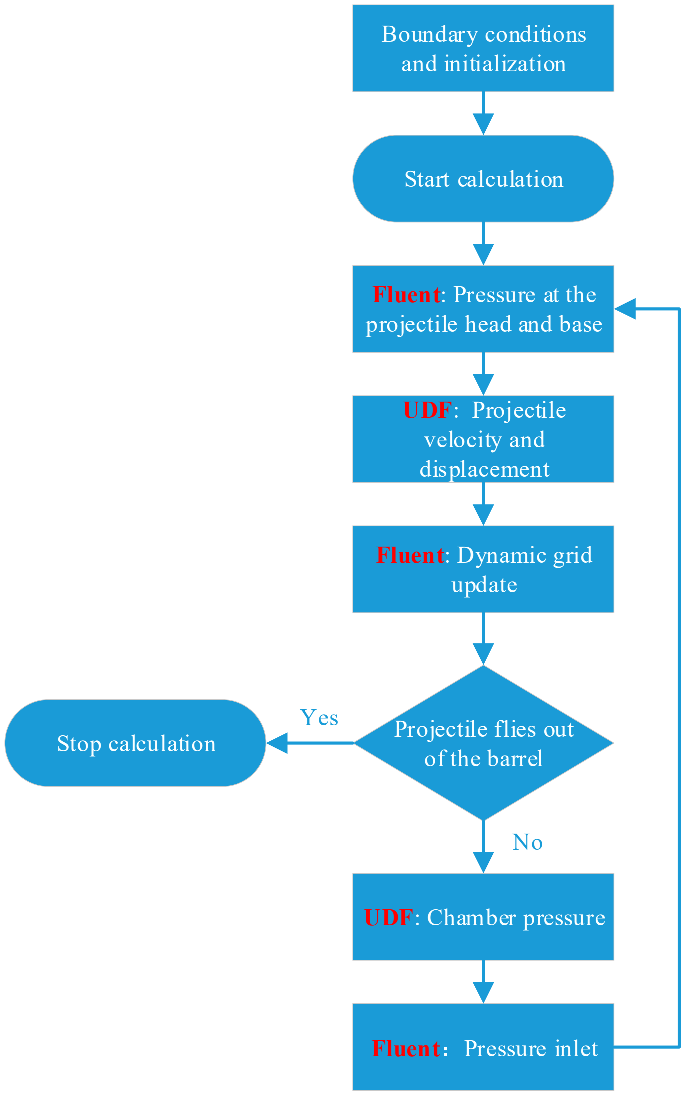

Figure 2. The coupling solution of FLUENT and UDF.

The calculation domain is shown in Figure 3. The inlet pressure is calculated in the simulation by determining the pressure in the chamber. The outlet pressure is p_0 and the temperature is T_0. For all numerical calculation examples in this paper, p_0 is set to 101,325 Pa and T_0 is set to 300 K. The motion of the projectile along the axis of the barrel is taken into account and treated as a moving rigid body.

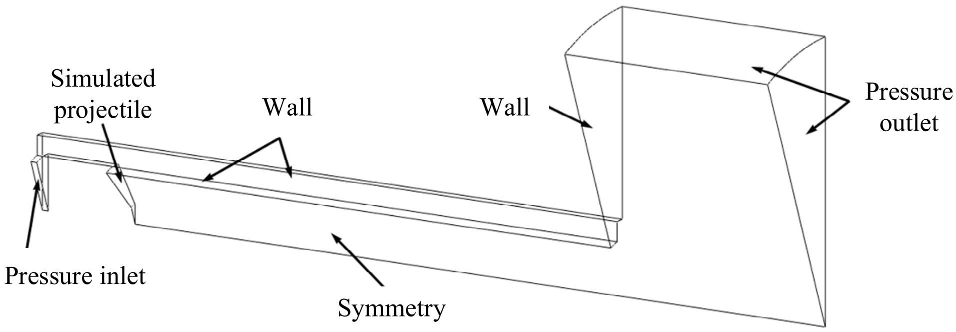

Figure 3. Schematic diagram of calculation domain.

Based on the aforementioned concept and methodology, a numerical validation is performed. Projectile *E*'s experimental finding from reference [23] is repeated. The numerical and experimental findings of the axial displacement of the gas-curtain are shown in Figure 4. The figure illustrates that the model built above is practicable because the average error between simulation and experiment is no more than 4.86%.

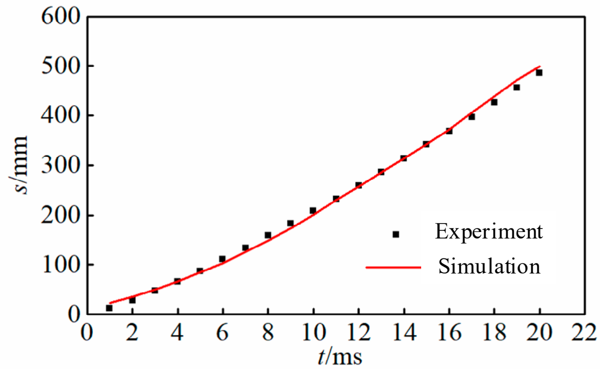

Figure 4. Axial displacement of the gas-curtain.

4. Results and Discussions

To achieve a highly efficient and low-resistance launch of an underwater ventilated launcher, the drag-reduction effect of the gas-curtain and time control of the interior ballistic must be fully considered. As mentioned earlier, coated propellant is used, in which the coating layer burns slowly to create the gas-curtain for draining off water. The propellant matrix burns quickly and it is mainly used to propel the projectile to achieve an ideal muzzle velocity.

The flow field and interior ballistic properties of the ventilated launch are examined in this research using the same charge under various starting conditions, primarily the initial injection pressure of the gas and the starting pressure of the projectile. The initial injection pressure varies from 8 to 20 MPa, while the starting pressure of the projectile varies from 30 to 50 MPa.

4.1. Influence of Gas Injection Pressure

The underwater ventilated launch procedure is compared using the same propellant at the four different gas injection pressures: 8, 10, 15, and 20 MPa. Figure 5 shows the evolution process of the pressure within a symmetrical cross-section when the gas injection pressure (P_0) is 8, 15, and 20 MPa. The jet contour curve is depicted by the black dashed line.

The high-pressure region in the internal flow field inside the barrel is situated close to the jet head at 3.0 ms, as depicted in the figure. The axial expansion displacement of the jet, the pressure inside the high-pressure zone, and the separation between the high-pressure zone and the entrance of the barrel all increase as the gas injection pressure rises. The pressure inside the barrel is significantly lower at 6.0 ms than it was at the previous moment, but the high-pressure zone distribution varies under the three working conditions. When P_0 = 8 MPa, the high-pressure zone forms close to the jet head. When P_0 = 15 MPa, a banded high-pressure zone forms close to the projectile head (s = 20 mm). At P_0 = 20 MPa, two banded high-pressure zones form in the barrel near s = 30 mm and s = 200 mm downstream from the projectile. At 8.0 ms, multiple banded high-pressure zones also developed in the barrel with the gas injection under the working parameters of P_0 = 8 MPa and P_0 = 10 MPa. As can be observed, a banded high-pressure zone forms in the barrel sooner the higher the gas injection pressure.

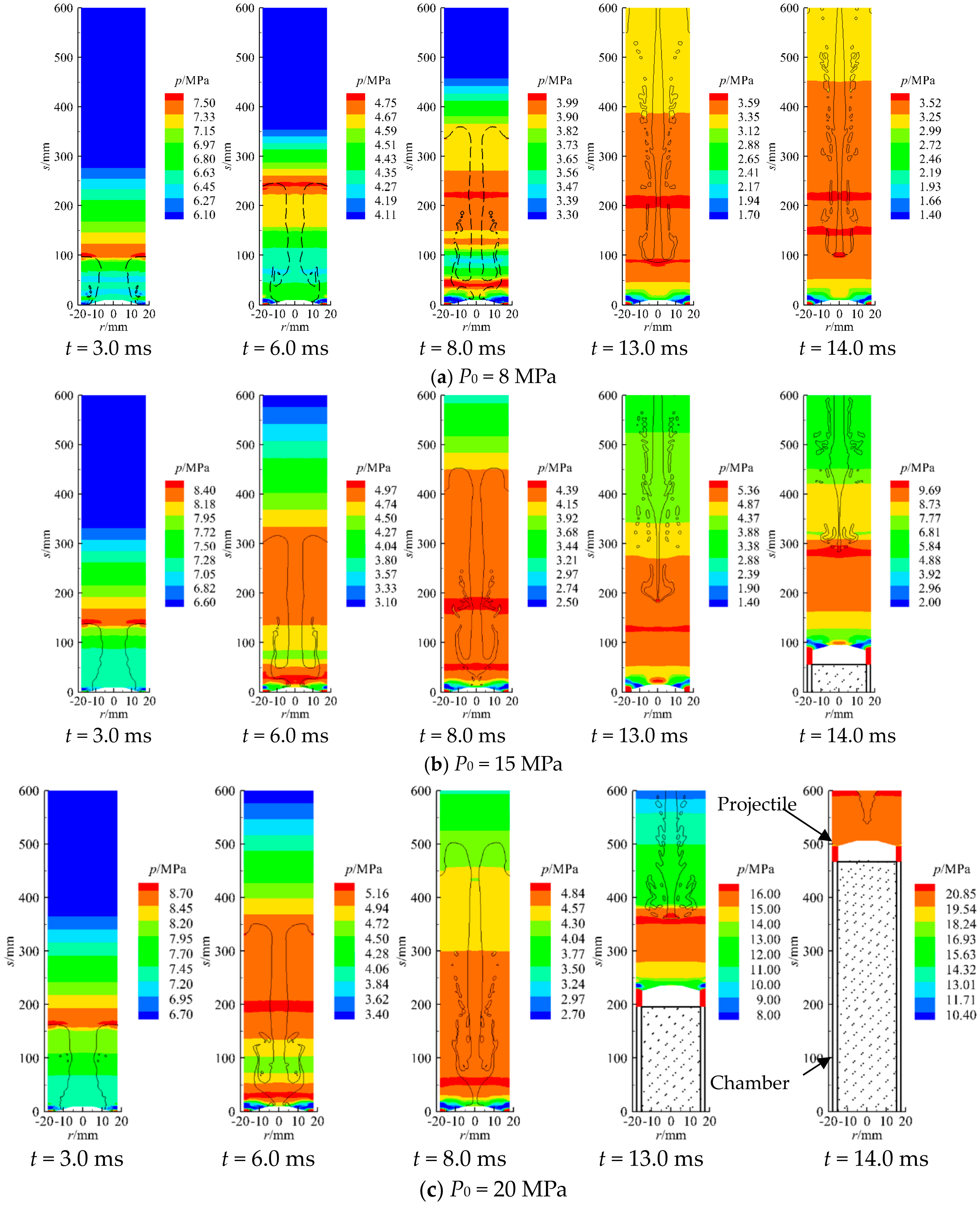

Figure 5. Evolution process of pressure within a symmetric cross-section.

At 13.0 ms, the pressure within the barrel is still falling compared to the prior time when P_0 = 8 MPa, but it is rising compared to the preceding moment when P_0 = 15 MPa and P_0 = 20 MPa. This is due to the fact that the projectile has already begun to travel in both working scenarios, which enhances the interaction between the projectile and the gas-curtain. At 14.0 ms, the local high-pressure zone right above the projectile head is still there under the operating condition P_0 = 15 MPa, but the pressure above the projectile head has tended to be dispersed evenly when P_0 = 20 MPa. It is clear that the initial injection pressure influences the gas-curtain expansion process as well as the projectile motion, which in turn influences the characteristics of pressure distribution inside the barrel.

The pressure inside the symmetrical section at gas injection pressures of 8, 15, and 20 MPa with projectile velocity of 258.0 m/s are shown in Figure 6. It can be seen that the higher the gas injection pressure, the higher the pressure inside the tube when the projectile speed is the same, and the weaker the projectile acceleration ability. According to the figure, the maximum pressure inside the barrel rises from 12.74 to 17.79 MPa when the gas injection pressure rises from 8 to 20 MPa, and the projectile displacement also somewhat increases. As can be observed, the ability of the projectile to accelerate is weaker the greater the gas injection pressure, the higher the pressure inside the barrel with the same projectile velocity. Additionally, it can be seen that the distance between the gas-curtain depression and the projectile head increases with decreasing initial injection pressure of the gas.

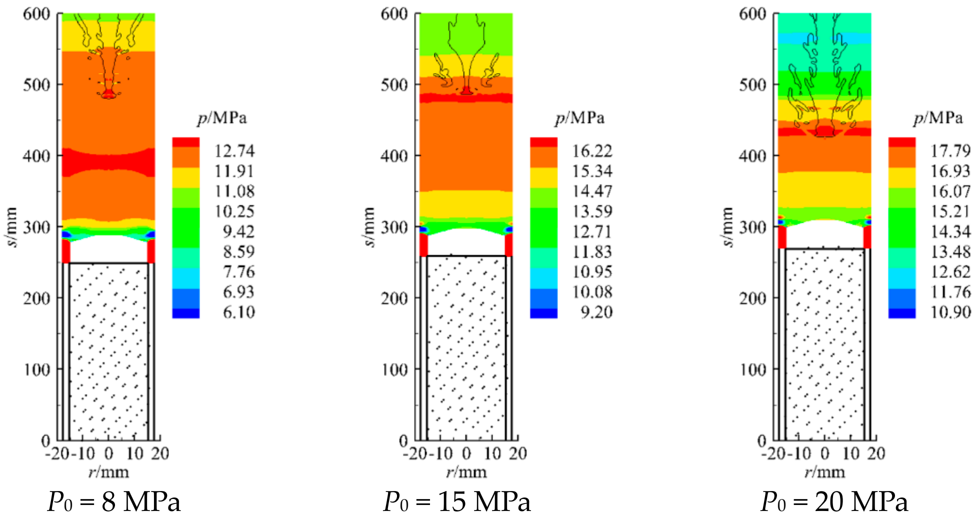

Figure 6. Pressure distribution within a symmetrical cross-section (v_p = 258.0 m/s).

According to numerical simulation, the projectile starts to move at 15.8, 14.7, 12.5, and 10.8 ms under the four different operating conditions, respectively. The variation curve for the axial expansion displacement of the gas-curtain under the four different gas injection pressures is shown in Figure 7, together with the gas volume fraction in the barrel during the drainage stage. The gas volume fraction in the barrel gradually increases along with the axial expansion displacement of the gas-curtain as the gas injection pressure rises. Additionally, the growth rate for both the axial expansion speed of the gas-curtain and the gas volume fraction in the barrel gradually rises.

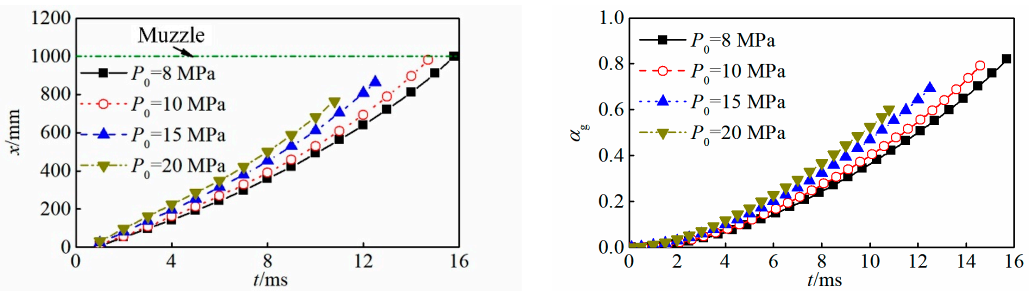

(**a**) Axial displacement of the gas-curtain (**b**) Gas volume fraction in the barrel

Figure 7. Gas-curtain drainage characteristics under different gas injection pressures.

The gas-curtain drainage parameters under different gas injection pressures are given in Table 1. Based on Figure 7 and Table 1, it can be seen that as the gas injection pressure rises, the projectile movement time advances and the duration of the gas-curtain drainage stage falls from 15.8 to 10.8 ms, resulting in a reduction in the axial expansion displacement of the gas-curtain before the projectile starts. The integral number for the combustion gas inside the barrel falls from 0.83 to 0.60 as the gas-curtain expansion becomes more insufficient, although the average gas-curtain drainage rate continuously rises from 41.00 to 43.36 g·ms^{-1}.

Table 1. Gas-curtain drainage parameters under different gas injection pressures.

NO.	P_0/MPa	t_p/ms	s_p/mm	α_g	η/g·ms^{-1}
1	8	15.8	1000.00	0.83	41.00
2	10	14.7	981.50	0.80	42.47
3	15	12.5	862.29	0.69	43.08
4	20	10.8	764.05	0.60	43.36

The pressure at the projectile head for the four different gas injection pressures is displayed in Figure 8. According to the figure, when different injection pressures are used, the surface pressure at the projectile head first rises and then falls as the projectile moves. The surface pressure of the projectile gradually rises as the gas injection pressure rises, but there is little difference in the maximum surface pressure under P_0 = 8 MPa and P_0 = 10 MPa, P_0 = 15 MPa, and P_0 = 20 MPa. Under the four working conditions, the projectile's maximum surface pressure is 19.65, 20.76, 22.24, and 22.81 MPa, respectively.

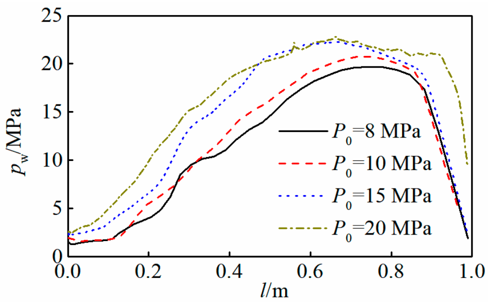

Figure 8. Surface pressure of the projectile under different gas injection pressures.

The interior ballistic curves for the ventilated launch under varied gas injection pressures are shown in Figure 9. As seen in Figure 9a, during the propellant coating's combustion phase, the chamber pressure rises concurrently with the gas injection pressure, though more slowly. The maximum pressure inside the chamber does not change much, but the propellant coating burns sooner. The timing of the complete launch process is reduced from 20.4 to 15.5 ms as indicated in Figure 9b, and as a result, the final velocity of the projectile at the muzzle is reduced from 360.6 to 338.4 m/s. Both the whole interior ballistic time and the muzzle velocity are decreased by 24.0% and 6.1%, respectively.

The interior ballistic properties of the underwater ventilated launch at the four different gas injection pressures are shown in Table 2. For the four different gas injection pressures, the change of the maximum chamber pressure is negligible. The duration of a single launch and the muzzle velocity of the projectile increase with decreasing gas injection pressure. It should be noted that the increase in the projectile's muzzle velocity reduces when the gas injection pressure steadily drops from 20 to 8 MPa. Based on Table 1, it can be seen that when the gas injection pressure decreases, the average gas-curtain drainage rate steadily declines, but as the gas used for drainage grows, there is more than enough drainage as a result. The internal ballistics time for a single launch is inversely related to the initial gas injection pressure under specific charge and injection structure circumstances.

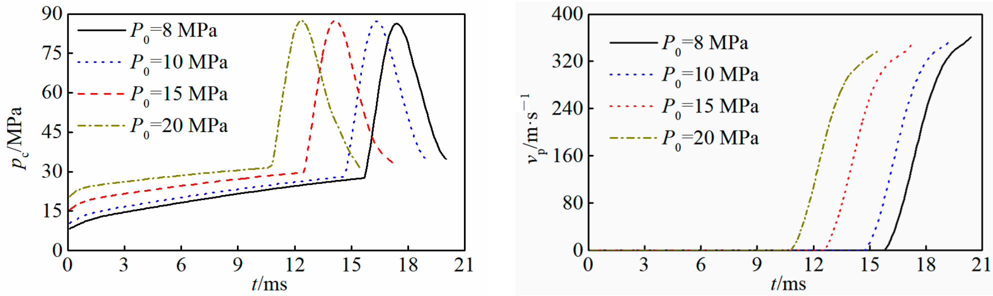

(**a**) chamber pressure (**b**) projectile velocity

Figure 9. Interior ballistic curves under varied gas injection pressures.

Table 2. The interior ballistic properties at the four different gas injection pressures.

No.	P_0/MPa	$p_{c,max}$/MPa	t_0/ms	$v_{p,0}$/m·s^{-1}
1	8	86.3	20.4	360.6
2	10	87.1	19.3	358.0
3	15	87.4	17.2	347.7
4	20	87.4	15.5	338.4

4.2. Influence of Projectile Starting Pressure

In this section, the interior ballistic properties of the ventilated launch at projectile starting pressures (P_j) of 30, 40, and 50 MPa are compared and analyzed. P_0 = 8 MPa is the chosen gas injection pressure.

The interior ballistic curves for the underwater ventilated launch at various projectile starting pressures are depicted in Figure 10. The maximum chamber pressure rises from 86.34 to 102.7 MPa, an increase of 18.9%, as the projectile starting pressure rises from 30 to 50 MPa, while the muzzle velocity of the projectile only increases from 360.58 to 385.42 m/s, an increase of 6.9%. The starting time of the projectile is delayed as the projectile starting pressure increases. Under the three operating conditions, the time needed for a single launch is not noticeably different.

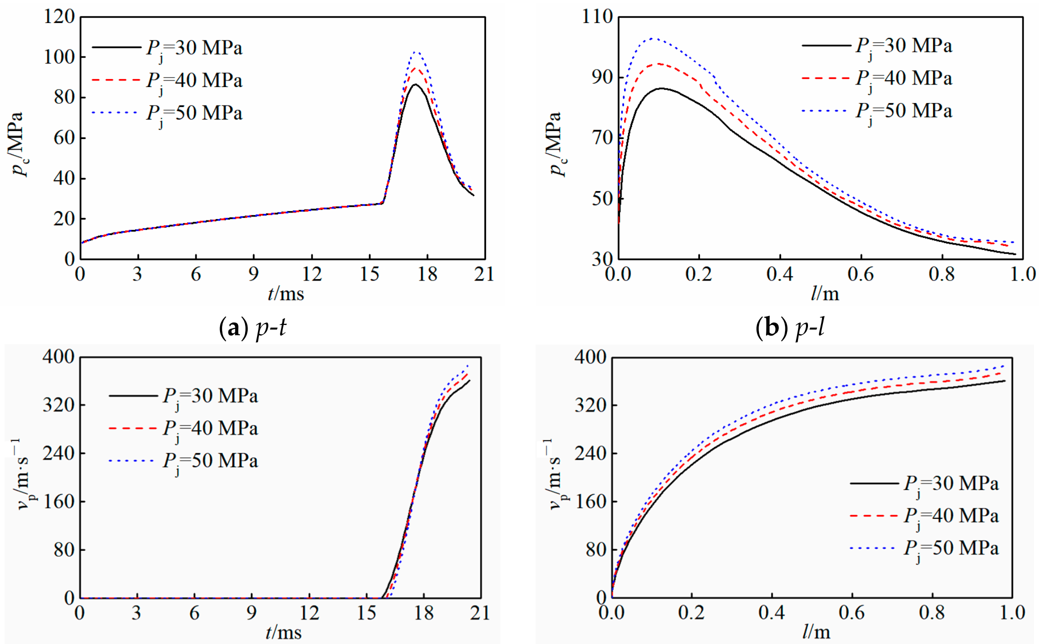

(**a**) *p-t* (**b**) *p-l*

(**c**) *v-t* (**d**) *v-l*

Figure 10. Interior ballistic curves under different projectile starting pressures.

Figure 11 depicts the relationships between surface pressure and displacement of the projectile under different projectile starting pressures. The figure shows that the larger the projectile starting pressure, the farther back the place where the surface pressure abruptly rises, and the higher the peak pressure on the surface of the projectile. This is due to the fact that the gas near the projectile can have more time to expand as the starting pressure rises, but the amount of gas downstream from the entire gas-curtain also rises. The maximum surface pressure rises from 19.65 to 22.00 MPa, an increase of 11.2%, when the projectile's starting pressure rises from 30 to 50 MPa. It is clear from this observation that the increase in surface pressure of the projectile is less significant than the increase in maximum chamber pressure, which further explains why the projectile's muzzle velocity increased.

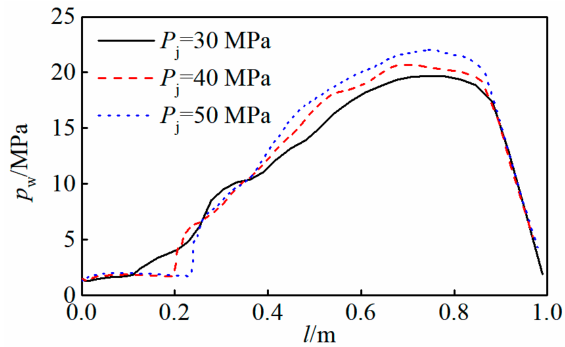

Figure 11. Relationships between surface pressure and displacement of the projectile.

5. Conclusions

A two-phase flow and interior ballistic coupling model is developed and validated based on the underwater low-resistance launch concept, and the effect of starting conditions on the internal flow field and interior ballistic characteristics of underwater ventilated launch are examined. The results found are as follows.

(1) A solid foundation has been established for future simulation designs of underwater ventilated launchers owing to the coupling model developed for underwater ventilated guns, which produces a simulation error in the axial expansion displacement of the jet head of no more than 4.86%.

(2) According to the operating conditions described in this paper, the burning duration of the propellant coating layer is decreased with an increase in gas injection pressure, and the gas-curtain's drainage impact is lessened as a result. The maximum chamber pressure does not significantly change when the gas injection pressure rises from 8 to 20 MPa, although the projectile's muzzle velocity drops by roughly 6.2%. The drainage effect of the gas-curtain is not significantly altered by increasing the projectile's starting pressure from 30 to 50 MPa. However, as the pressure differential between the projectile's front and back widens, the projectile's acceleration and motion resistance both slightly increase. The projectile's muzzle terminal velocity increases by 6.9%, and the chamber pressure significantly increases by 18.9%.

(3) The starting pressure of the projectile has a more pronounced effect on the internal ballistics performance of the underwater ventilated launch than the gas injection pressure does.

Furthermore, the matching design of gas injection pressure and projectile starting pressure to boost the launching effectiveness and interior ballistic performance of underwater ventilated launchers is one of the future directions for this work.

Author Contributions: Conceptualization, X.Z. and Y.Y.; methodology, X.Z.; formal analysis, X.Z. and Y.H.; investigation, X.Z. and Y.H.; resources, X.Z. and Y.Y.; data curation, X.Z. and Y.H.; writing—original draft preparation, X.Z. and Y.H; writing—review and editing, X.Z. and Y.Y.; supervision, X.Z.; project administration, X.Z.; funding acquisition, X.Z. All authors have read and agreed to the published version of the manuscript.

Funding: This research was funded by the China Postdoctoral Science Foundation (Grant Number 2020M681596).

Institutional Review Board Statement: Not applicable.

Informed Consent Statement: Not applicable.

Data Availability Statement: The data in this article are true and valid. The data presented in this study are available in this article and [23].

Conflicts of Interest: The authors declare no conflict of interest.

References

1. Zhang, N.; Zhao, Y.; Wei, H.; Chen, G. Experimental study on the influence of air injection on unsteady cloud cavitating flow dynamics. *Adv. Mech. Eng.* **2016**, *8*, 1–7. [CrossRef]
2. Kim, S.; Lee, J.; Lee, H.; Lim, J.; Cho, J. Effect of rotating, non-axisymmetric cavitator on supercavity size. *J. Mech. Sci. Technol.* **2022**, *36*, 3437–3447. [CrossRef]
3. Pham, V.-D.; Hong, J.-W.; Ahn, B.-K. Experimental investigation of combustion hot-gas ventilated supercavitation. *Int. J. Nav. Archit. Ocean. Eng.* **2022**, *14*, 100477. [CrossRef]
4. Qi, X.B.; Yuan, X.L.; Xu, B.C.; Wang, J.W.; Li, R.J. Research on Ignition Timing Choice for Near-Tube Underwater Vertical Launching Missile. *J. Propuls. Technol.* **2019**, *40*, 1449–1457. (In Chinese)
5. Corwel, C.; Zoghbi, G.; Webb, S.; Dutta, A. Design and Control of an Underwater Launch System. *IEEE Access* **2020**, *8*, 38633–38649. [CrossRef]
6. Yuan, J.; Zhu, J.; Xu, J.; Sun, X.; Zhang, X.; Zheng, X. Trajectory prediction of underwater launch equipment based on varying flow coefficient. *Ocean. Eng.* **2023**, *273*, 113814. [CrossRef]
7. Chen, J.; Wang, C.M.; Di, C.A.; Liu, G.L. Interior Ballistic Calculations of an Under Water Gun at Various Depths. *Acta Armamentarii* **2002**, *23*, 462–464. (In Chinese)
8. Fu, J.; Howard, R.J.; Rapp, J.W.; Paulic, A. Underwater Gun Comprising a Plate-Type Barrel Seal. U.S. Patent No. 7,874,091, 25 January 2011.
9. Sun, P.; Xie, Z.J.; Yang, Z.; Lan, W.B. Analysis of the Influence of the Inlet of the Barrel on the Shooting. *J. Ordnance Equip. Eng.* **2018**, *39*, 68–72. (In Chinese)
10. Hu, Z.T.; Yu, Y.G. Study on Three-Dimensional Expansion Characteristics of Four Wall Combustion-Gas Jets in Confined Liquid Space. *Acta Mech. Sin.* **2017**, *33*, 341–355. [CrossRef]
11. Zhou, L.L.; Yu, Y.G. Study on the gas-curtain generation characteristics by the multiple gas jets in a liquid-filled tube. *Appl. Ocean. Res.* **2017**, *64*, 249–257. [CrossRef]
12. Hu, Z.T.; Yu, Y.G. Expansion Characteristics of Multiple Wall Jets in Cylindrical Observation Chamber. *Appl. Therm. Eng.* **2017**, *113*, 1396–1409. [CrossRef]
13. Zhao, J.J.; Yu, Y.G. Flow Structure of Conical Distributed Multiple Gas Jets Injected into a Water Chamber. *J. Mech. Sci. Technol.* **2017**, *31*, 1683–1691. [CrossRef]
14. Zhou, L.L.; Yu, Y.G. Study on Interaction Characteristics between Multi Gas Jets and Water During the Underwater Launching Process. *Exp. Therm. Fluid Sci.* **2017**, *83*, 200–206. [CrossRef]
15. Hu, Y.B.; Yu, Y.G.; Zhang, X.W. Groove structure on the drainage characteristics of the gas curtain. *Ocean. Eng.* **2022**, *243*, 110280. [CrossRef]
16. Zhang, X.W.; Yu, Y.G.; Zhou, L.L. Numerical study on the multiphase flow characteristics of gas curtain launch for underwater gun. *Int. J. Heat Mass Transf.* **2019**, *134*, 250–261. [CrossRef]
17. Mulbah, C.; Kang, C.; Mao, N.; Zhang, W.; Shaikh, A.R.; Teng, S. A Review of VOF Methods for Simulating Bubble Dynamics. *Prog. Nucl. Energy* **2022**, *154*, 104478. [CrossRef]
18. Sadeghi, H.; Tavoularis, S. Numerical Studies of Gas Pull-Through and Liquid Entrainment in Gas–Liquid Flows through Multi-Branch Manifolds. *Int. J. Multiph. Flow* **2022**, *155*, 104173. [CrossRef]
19. Wang, Z.; He, Y.; Duan, Z.; Huang, C.; Yuan, Y.; Li, M.; Liu, S. Effects of Rolling Motion on Transient Flow Behaviors of Gas-Liquid Two-Phase Flow in Horizontal Pipes. *Ocean. Eng.* **2022**, *255*, 111482. [CrossRef]
20. Shao, C.; Bao, N.; Wang, S.; Zhou, J. Study on the prediction method and the flow characteristics of gas-liquid two-phase flow patterns in the suction chamber. *Int. J. Numer. Methods Heat Fluid Flow* **2022**, *32*, 2700–2718. [CrossRef]
21. Cheng, C.; Zhang, X.B. Numerical modeling and investigation of two-phase reactive flow in a high-low pressure chambers system. *Appl. Therm. Eng.* **2016**, *99*, 244–252. [CrossRef]

22. Cheng, C.; Wang, G.; Huang, X.; Zhang, X. Numerical Investigation on the Gas-Solid Flow in Blast Flow Fields Induced by a High-Speed Body. *Propellants Explos. Pyrotech.* **2023**, *48*, e2022001. [CrossRef]
23. Zhang, X.W.; Yu, Y.G.; Hu, Y.B. Experimental Study on Gas–Liquid–Solid Interaction Characteristics in the Launch Tube. *J. Mar. Sci. Eng.* **2022**, *10*, 1239. [CrossRef]

Disclaimer/Publisher's Note: The statements, opinions and data contained in all publications are solely those of the individual author(s) and contributor(s) and not of MDPI and/or the editor(s). MDPI and/or the editor(s) disclaim responsibility for any injury to people or property resulting from any ideas, methods, instructions or products referred to in the content.